Correlated distributions in the photodissociation of HNCO to NH($X\,^3\Sigma^-$, $a^1\Delta$) + CO($X\,^1\Sigma^+$) near the barrier on S_1

Thierry Droz-Georget [a], Mikhail Zyrianov [a], Hanna Reisler [a,*], David W. Chandler [b]

[a] *Department of Chemistry, University of Southern California, Los Angeles, CA 90089-0482, USA*
[b] *Combustion Research Facility, Sandia National Laboratories, Livermore, CA 94550, USA*
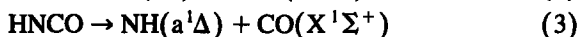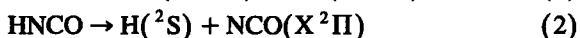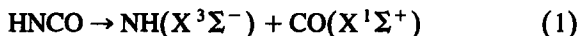
Abstract

The photodissociation of HNCO is examined at 230.1 nm, near the threshold to NH($a^1\Delta$) + CO($X\,^1\Sigma^+$). CO products are generated from NH($X\,^3\Sigma^-$) + CO($X\,^1\Sigma^+$) and NH($a^1\Delta$) + CO($X\,^1\Sigma^+$). Although the two contributions *overlap spectroscopically*, they are *resolved in velocity space* when using photofragment ion imaging. For both channels the CO rotational distribution is cold and non-statistical. A high resolution variant of imaging is employed to obtain NH($a^1\Delta$) distributions correlating with specific J_{CO} levels. Combining these measurements with NH($a^1\Delta$) photofragment yield spectra and rotational distributions, we establish that decomposition to NH($a^1\Delta$) + CO($X\,^1\Sigma$) evolves over a small barrier on S_1, estimated at 400–600 cm^{-1}. © 1997 Elsevier Science B.V.

1. Introduction

Recently, significant progress towards the understanding of the photodissociation of HNCO following S_1 excitation has been achieved [1–17]. Although HNCO is only a four-atomic molecule, unravelling its dissociation mechanism is complicated by the participation of at least three potential energy surfaces (S_0, S_1 and T_1) and the presence of three competitive pathways [10–13]:

$$HNCO \rightarrow NH(X\,^3\Sigma^-) + CO(X\,^1\Sigma^+) \qquad (1)$$
$$HNCO \rightarrow H(^2S) + NCO(X\,^2\Pi) \qquad (2)$$
$$HNCO \rightarrow NH(a^1\Delta) + CO(X\,^1\Sigma^+) \qquad (3)$$

In what follows NH($X\,^3\Sigma^-$) and NH($a^1\Delta$) will be

denoted by ^{3}NH and ^{1}NH, respectively. All three channels are active near the threshold to channel (3) [11,13].

In a series of studies carried out a decade ago, Chandler and coworkers determined ^{1}NH and CO product state distributions at several photolysis wavelengths [2], and concluded that channel (3) evolves via direct dissociation on S_1. Since then, new data have become available that call for a re-examination of this scenario. Specifically, the threshold to dissociation via channel (3) has been revised upward to $D_0(^1NH + CO) = 42765 \pm 25$ cm^{-1} (233.8 nm) [12], and a second source of CO, i.e., channel (1) {$D_0(^3NH + CO) = 30080$ cm^{-1} (332.4 nm) [11,13]}, has been shown to be important at some of the wavelengths investigated previously. Recently, Reisler and coworkers have proposed,

---

* Corresponding author. E-mail: reisler@chem1.usc.edu

based on their measured ^{1}NH rotational state distributions obtained with jet-cooled samples, that at least near its threshold, channel (3) evolves on S_0 following $S_1 \rightarrow S_0$ internal conversion (IC) [10]; at shorter wavelengths, e.g., 217 nm, dissociation on S_1 is dominant [8,11,12]. The data suggest that a change in mechanism to direct dissociation on S_1 occurs around 231–225 nm [11]. Re-interpretation of the results obtained by Chandler and coworkers by using the revised value of $D_0(^1$NH + CO$)$ is not possible, since it is now established that at photolysis wavelengths ≥ 230 nm, channel (1) contributes significantly to the CO signal [13]. For example, at 230 nm production of CO via channel (1) is approx. 5-fold larger than via channel (3), and thus the previous CO measurements at this wavelength contain unknown contributions from the former channel.

In order to reconcile the earlier observations and determine the mechanism near the threshold to channel (3), it is necessary to distinguish between the contributions of channels (1) and (3) to the observed CO signal. The photofragment ion imaging technique is particularly suitable for this task [18]. In addition to providing selectivity in the frequency domain using resonantly enhanced multiphoton ionization (REMPI) for fragment detection, it also enables resolution in velocity space, allowing discrimination between fast and slow products. Since the thresholds to channels (1) and (3) differ by > 12000 cm^{-1}, this can be easily accomplished in the present case.

In this Letter we report a photofragment imaging study of the 230.1 nm photodecomposition of HNCO and determine the CO rotational distribution correlated solely with ^{1}NH. In addition, the rotational state disbributions of the ^{1}NH counter-fragment correlated with selected rotational levels of CO are obtained by using a high resolution variant of the imaging technique — velocity map imaging [19]. These measurements establish that at 230.1 nm channel (3) evolves mainly via dissociation on S_1. By combining these results with ^{1}NH photofragment yield spectra and rotational state distributions obtained previously near the channel (3) threshold [10], we are able to place the S_1 barrier to dissociation at 400–600 cm^{-1} above $D_0(^1$NH + CO$)$.

2. Experimental techniques

2.1. Photofragment ion imaging

The imaging arrangement is similar to the one developed by Chandler and Houston [18], and is described in detail elsewhere [12]. In brief, it consists of an ion-acceleration stage, a 60 cm long drift-tube, a position-sensitive detector and a CCD camera that monitors a phosphor screen coupled to a MCP particle-multiplier. A doubly-skimmed pulsed molecular beam containing 2% HNCO seeded in 1 atm He propagates in-line with the detector and enters the acceleration region through a hole in the repeller plate. HNCO ($T_{rot} \leq 5$ K) is photolysed with pulsed, linearly polarized and focused ($f = 15$ cm) laser radiation (0.5–1.5 mJ) intersecting the molecular beam at right angle. CO products are interrogated by $2 + 1$ REMPI via the Q-branch of the B $^1\Sigma^+ \leftarrow \leftarrow$ X $^1\Sigma^+$ transition at 230.1 nm ($\leftarrow \leftarrow$ denotes two-photon absorption). All imaging data reported here are from "one-color" experiments, i.e., HNCO photolysis and product detection are carried out at the same wavelength.

2.2. Velocity map imaging

Results on correlated ^{1}NH rotational distributions were obtained with a modified ion-optics configuration based on a scheme proposed recently by Parker et al. for velocity focusing [19]. A repeller, an open extractor electrode (with a 50 mm hole), and an open ground electrode (with a 25 mm hole) are used instead of the conventional setup — repeller and ground grid electrode. At an optimal voltage ratio for the repeller and extractor plates, all ions with the same initial velocity are focused to the same spot on the MCP detector (velocity map imaging). This setup removes grid distortions and, most importantly, image blurring due to the finite size of the laser/molecular beam interaction volume, thus increasing the velocity resolution by nearly an order of magnitude at high ion acceleration voltages (e.g. $\Delta v/v = 1\%$ at 200 V/cm) [20]. Typical acceleration voltages used in our study are < 30 V/cm, corre-

sponding to flight times of ≈ 20 μs. At these long times the resolution is poorer and is limited by the photofragment recoil and molecular beam velocity spread as well as by the mechanical precision of the lens assembly.

2.3. CO REMPI spectra from imaging data

Eighty images recorded at various wavelengths covering the relevant spectral region ($J_{CO} = 0$–60) of the Q-branch of the B ← ← X system near 230.1 nm were used to reconstruct the CO REMPI spectrum. For each image the integrated ion signal, normalized to the number of laser shots (typically 150–6000), represents the spectral intensity at the image's wavelength [1]. Note that the CO REMPI spectrum shown in Fig. 1(c) is not structured because: (i) the Q-branch bandhead is severely collapsed [21], and therefore, with the bandwidth of our laser (≈ 0.2 cm^{-1}) the spectrum exhibits a smooth envelope at least up to $J_{CO} = 18$–20; (ii) the CO rotational levels associated with channel (1) are significantly Doppler broadened due to a large translational energy release, (the linewidth at the bandhead is estimated at ≈ 1 cm^{-1} FWHM). Simulations show that the spectrum should remain structureless up to the highest J_{CO} observed in our experiment, which justifies representating the CO spectrum by a relatively small number of discrete points. For $J_{CO} < 25$, images were recorded at fixed laser wavelengths; higher J's, on the other hand, were probed while scanning the laser by ≈ 0.02 nm during image acquisition.

2.4. Laser induced fluorescence (LIF) measurements

The global ^1NH rotational distributions were measured in a separate apparatus as described elsewhere [22]. Jet-cooled HNCO ($T_{rot} \approx 10$ K) was photolysed with the output of a tunable dye laser. ^1NH fragments were probed under non-saturated conditions by LIF via the c $^1\Pi$ ← a $^1\Delta$ transition, using a second laser. The observed spectral line intensities
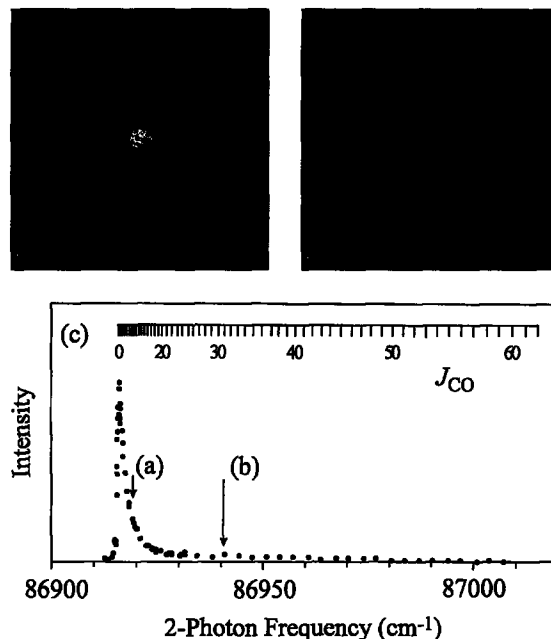
Fig. 1. Images of CO($v = 0$) from HNCO following 230.1 nm photolysis: (a) $J_{CO} \approx 10$ and (b) $J_{CO} \approx 30$. (c) 2+1 REMPI spectrum of CO recorded via the Q-branch of the B $^1\Sigma^+$ ← ← X $^1\Sigma^+$ transition; each data point corresponds to an image; arrows indicate the positions at which the images in (a) and (b) were taken.

were normalized by the line strength factors to obtain J_{NH}-level populations.

3. Results

3.1. Velocity resolved CO REMPI spectra

Fig. 1(a) and (b) show representative images, i.e., 2D projections of the 3D photofragment velocity distributions of CO products from photolysis at 230.1 nm $-$ 690 cm^{-1} above $D_0(^1NH + CO)$ and 13375 cm^{-1} above $D_0(^3NH + CO)$. $J_{CO} \approx 10$ and $J_{CO} \approx 30$ were monitored for (a) and (b), respectively, using the conventional imaging ion optics with a homogeneous extraction field. For the reasons discussed above, individual rotational lines are not well resolved, and therefore only approximate assignments can be given.

The image for $J_{CO} \approx 10$ exhibits a clear bimodality in the photofragment velocity distribution. Based on energy conservation, the inner, more intense area is correlated with CO generated via the $^1NH + CO$
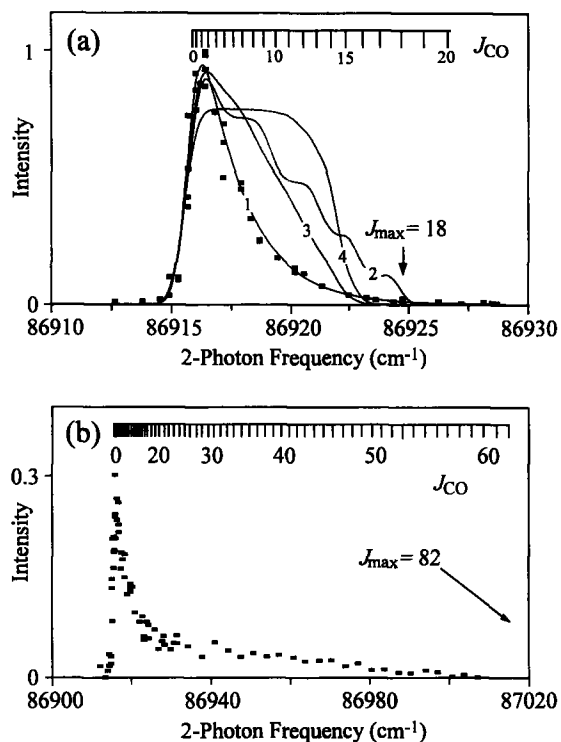
Fig. 2. (a) 2 + 1 REMPI spectrum of CO($v = 0$) correlated with
^{1}NH. Solid lines show fits to various models: curve "1" results
from a fit to a Gaussian shaped rotational distribution peaking at
$J = 0$ with $J = 14$ FWHM; curve "2" represents an unrestricted
PST distribution; curve "3" is the PST result with an impact
parameter restricted to $b_{max} = 2$Å and curve "4" incorporates, in
addition, the experimental ^{1}NH distribution (see text for details).
(b) 2 + 1 REMPI spectrum of CO($v = 0$) correlated with ^{3}NH.
The intensity scales reflect the relative intensities of the CO
REMPI signals originating in the singlet and triplet channels. Note
the different frequency scales in (a) and (b).

channel ("singlet" CO), while the weaker feature
extending up to the highest velocities is associated
with co from the ^{3}NH + CO channel ("triplet"
CO). For $J_{CO} > 18$ the singlet channel is no longer
accessible, while the energetic cut-off for the triplet
channel is at $J_{CO} = 82$. As a consequence, images
recorded in the interval $18 < J_{CO} < 82$ are unimodal
as displayed for $J_{CO} \approx 30$ in Fig. 1(b). Note that the
reduction in the image radius by $\approx 6\%$ in going
from $J_{CO} \approx 10$ to $J_{CO} \approx 30$ reflects the decrease in
available energy.

The integrated signal for an image (both singlet
and triplet contributions), normalized to its acquisi-
tion time, represents the relative intensity of the
CO(v, J) REMPI signal at each wavelength. Fig.

1(c) shows a compilation of integrated intensities
obtained from 80 different images of CO($v = 0$) as a
function of the 2-photon frequency, which is equiva-
lent to the CO($v = 0$) REMPI spectrum. The two
arrows indicate the positions at which the images in
Fig. 1(a) and (b) were recorded. For images taken at
$J_{CO} > 57$ the signal level drops below our detection
limit.

The different spatial distributions of CO associ-
ated with the singlet and triplet channels enable us to
determine their separate contributions to the total
signal intensity. Integration of the intense, inner part
of an image yields the amount of CO from the
singlet channel, while subtraction of this number
from the total signal intensity gives the triplet chan-
nel contribution. A minor correction for the spatial
overlap of the two distributions near the center of the
image is taken into account. This procedure yields
the separated REMPI spectra for decomposition to
^{1}NH + CO and ^{3}NH + CO, as displayed in Fig. 2.
The arrows mark the highest J_{CO} allowed by energy
conservation [2].

3.2. "Singlet" CO rotational distribution

The 2 + 1 REMPI spectrum of CO produced via
the singlet channel consists of the Q-band of the CO
B $^1\Sigma^+ \leftarrow \leftarrow$ X $^1\Sigma^+$ transition, which is severely col-
lapsed. Consequently, it is impossible to extract line
intensities for individual CO rotational levels and
convert them to relative populations. A sensible way
to proceed is to use forward convolution. The best fit
to the experimental spectrum was obtained by de-
scribing the CO rotational distribution with a Gauss-
ian function centered at $J_{CO} = 0$ with FWHM = 14.
The fit is shown by the solid line marked "1" in
Fig. 2(a), obtained by describing the REMPI signal
intensity at frequency v by:

$$I(v) = C\sum_J (2J + 1)\Gamma(v - v_J)e^{\frac{-J^2}{\sigma^2}}$$

where v is the 2-photon frequency, v_J is the fre-

---

[2] In general, it is best to obtain the separate REMPI spectra by
first reconstructing the 3D velocity distribution for each image by
Abel inversion [18,23] followed by the integration steps. However,
most of the images described here have a signal to noise ratio
which is too low for a reliable Abel transformation (especially in
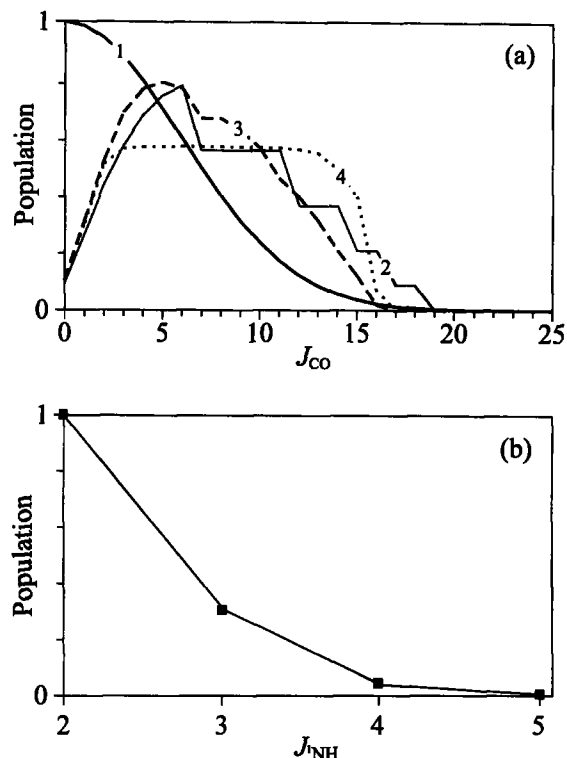the part generated by the triplet channel).

Fig. 3. (a) Model CO($v = 0$) rotational distributions for the various fits presented in Fig. 2(a); see caption of Fig. 2 for the description of the curves. Curve "1" provides the best fit to the experimental REMPI spectrum. (b) The experimental rotational distribution of ^{1}NH obtained via LIF with 230.0 nm photolysis.

quency of the Q$_J$ transition (B $^1\Sigma^+ \leftarrow \leftarrow$ X $^1\Sigma^+$), J denotes the CO rotational levels, $\Gamma(\nu - \nu_J)$ is an effective Gaussian line shape function of 0.3 cm^{-1} FWHM dominated by the laser bandwidth (the Doppler broadening for $J_{CO} = 0$ is < 0.2 cm^{-1}), C is an instrumental constant, and $\sigma = 8.3$ is the distribution width fit parameter. The rotational distribution is shown as trace "1" in Fig. 3(a), and the resulting REMPI spectrum is obtained by assuming that the rotational line strengths are proportional to the degeneracies of the rotational levels (total satura-

tion), and no other J-dependent intensity variations are important.

3.3. NH rotational distributions

^{1}NH rotational distributions were obtained at several photolysis wavelengths in the range 233.1–224.7 nm [135–1735 cm^{-1} above $D_0(^1$NH + CO)] from LIF spectra shown in fig. 4 of Ref. [10]. The ^{1}NH distribution obtained with 230.0 nm photolysis is presented in Fig. 3(b), and provides the conterpart of the CO distribution shown in Fig. 3(a). All the ^{1}NH distributions are cold, peaking at the lowest rotational level of the a$^1\Delta$ state, i.e. $J_{NH} = 2$, and Table 1 summarizes the relative ^{1}NH populations of $J_{NH} = 2$ and 3. For $E_{avl} > \approx 500$ cm^{-1} the rotational excitation increases rather monotonically with excess energy. However, near the channel (3) threshold, there is a distinct change — the distribution obtained with 231.7 nm photolysis is significantly "hotter" than the one obtained at 230.8 nm (vide infra).

3.4. Correlated ^{1}NH distributions

Displayed in Fig. 4(a) is a CO image obtained by using velocity map imaging. The image size was adjusted to display only the contribution from the singlet channel. In order to best define J_{CO}, i.e., minimize the overlap of CO rotational levels in the region of $J_{CO} \approx 0$–2, the image was recorded with the laser tuned to the red "tail" of the Q-band of the CO REMPI spectrum. At this wavelength, the laser frequency excites mainly CO fragments which move towards the laser light source (Doppler selection of products), and consequently the resulting image is asymmetric. Consistent with our previous measurements, which gave a recoil anisotropy parameter of -0.66 [12], the image exhibits clear anisotropy.

Following symmetrization, the image was transformed into the corresponding 3D recoil distribution

Table 1
^{1}NH rotational populations from HNCO dissociation obtained by LIF for six different photolysis wavelengths (λ_{diss})

λ_{diss} (nm)	233.1	231.7	230.8	230.0	229.4	224.7
E_{avl} (cm^{-1})	135	395	555	715	835	1735
$J_{NH} = 2$	1.00	1.00	1.00	1.00	1.00	1.00
$J_{NH} = 3$	0	0.34	0.16	0.30	0.28	0.51

E_{avl} denotes the available energy with respect to $D_0(^1$NH + CO). All values are normalized to the $J_{NH} = 2$ population and have an accuracy of 10%.
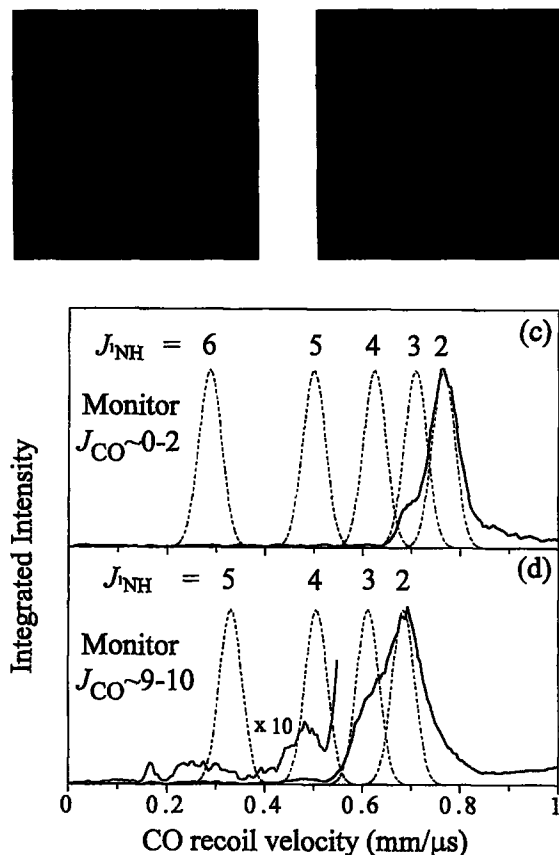
Fig. 4. (a) Experimental image of CO(v = 0) recorded for the red tail (low J's) of the REMPI spectrum shown in Fig. 1(b); only the low velocity part is monitored. The spot at the center of the image originates from residual CO introduced to adjust the ion-lens voltages for maximum focusing. (b) Abel transformation of the raw image in (a); the intensity discernible along the symmetry axis is not real but originates from experimental noise accumulated in the transformation process. (c) The corresponding velocity distribution (solid line). The positions of the correlated ^{1}NH rotational levels (assuming J_{CO} = 0) are given as dashed Gaussian curves; (d) The corresponding velocity distribution for an image taken at $J_{CO} \approx$ 9–10. The dashed Gaussian curves represent line positions and widths for J_{CO} = 9 (see text for details).

by means of Abel inversion [23]; a 2D cut through the reconstructed 3D distribution (containing the axis of cylindrical symmetry) is shown in Fig. 4(b). Visual inspection of Fig. 4(b) reveals that the translational energy release for CO(v = 0, $J \approx$ 0–2) is concentrated near the maximum value allowed by energy conservation. Thus, ^{1}NH produced in correlation with low J's of CO is rotationally cold, in

agreement with the global ^{1}NH distribution shown in Fig. 3(b).

More quantitative information on the ^{1}NH correlated distribution is gained from the CO recoil velocity distribution (solid line in Fig. 4c) obtained by integrating the 3D distribution along the polar angular coordinates θ and ϕ. The Gaussian-shaped dashed traces show schematically the positions of the correlated ^{1}NH rotational levels as calculated from energy conservation. Their estimated width is governed primarily by the uncertainty in the selection of CO rotational levels described above, i.e., $\Delta E_{avl} \approx$ 12 cm^{-1}, and the initial velocity spread in the HNCO beam. Obviously, the lowest J's of CO correlate mostly with J_{NH} = 2; J_{NH} = 3 contributing < 20% to the distribution. Although J_{NH} levels up to 6 are energetically allowed, J_{NH} = 3 is the highest observed level. The small signal at the highest velocities is due to fast recoiling CO from the triplet channel.

Fig. 4(d) presents a CO recoil velocity plot obtained from an image (not shown) recorded for $J_{CO} \approx$ 9–10,. The energetically allowed ^{1}NH rotational levels are J_{NH} = 2–5; the dashed Gaussian curves assume only a single CO rotational level, J_{CO} = 9, and therefore a slight offset increasing with J_{NH} is apparent between the model and the data. Again, the correlated ^{1}NH distribution is dominated by the J_{NH} = 2 contribution; however, the J_{NH} = 3 fraction has visibly increased relative to J_{NH} = 2, and even J_{NH} = 4 and 5 are noticeable. When comparing Fig. 4(c) and (d), it is important to realize that the width, due to the spectral overlap of J_{CO} levels, has almost doubled in going from $J_{CO} \approx$ 0–2 to $J_{CO} \approx$ 9–10; the shift in velocity between the two sets of data reflects the change in the available energy.

4. Discussion

4.1. Singlet channel dissociation at 230.1 nm

In previous work it was concluded that near its threshold, dissociation to ^{1}NH + CO proceeded on S$_0$ following IC. No significant barrier to decomposition was found experimentally [10] and in ab initio calculations [24]. For barrierless S$_0$ decomposition, the product state distributions are expected to be well described by statistical theories, and therefore, sev-

eral forms of phase space theory (PST) [25] have been compared with the experimental CO REMPI spectrum (Fig. 2a) and its rotational distribution (Fig. 3a). Unrestricted PST assumes that the probability of finding a product in a specified state is proportional to the number of ways the available energy (E_{avl}) can be distributed, subject only to energy and angular momentum conservation; curve "2" in Fig. 2(a) and Fig. 3(a) shows the results of such unrestricted PST calculation for $J_{HNCO} = 0$. Deviations from this distribution may arise from additional constrains, e.g., on the impact parameter and the co-fragment state distribution. Trace "3" in Fig. 2(a) and Fig. 3(a) displays results of a calculation in which the impact parameter is limited by $b_{max} = 2$ Å. The trace denoted by "4" incorporates an additional constraint — it imposes the experimentally determined ^{1}NH rotational distribution shown in Fig. 3(b). Obviously, none of these curves fits the data; although the CO rotational distribution extends to the maximum J allowed by energy conservation, it is quite cold, peaking at the lowest J's. We conclude that at 690 cm^{-1} above $D_0(^1$NH + CO) the CO rotational distribution is controlled by dynamics.

This conclusion is reinforced by the cold ^{1}NH rotational distribution shown in Fig. 3(b), as well as by the correlated ^{1}NH rotational distributions shown in Fig. 4(c) and (d). The latter display a low J–low J vs. a high J–high J correlation, which is characteristic of dissociation controlled by dynamics. Note also that the heights of the Gaussian curves in Fig. 4(c) and (d) representing the individual J_{NH} levels describe the unrestricted PST populations for $J_{HNCO} = 0$. The resulting large translational energy release inferred by energy balance is common in dissociations above a barrier, and thus we conclude that dissociation to ^{1}NH + CO proceeds on the S_1 potential energy surface over a barrier ≤ 690 cm^{-1}. The cold ^{1}NH and CO rotational distributions are typical of dynamics on a surface with little anisotropy in the angular NCO and HNC coordinates. In fact, the rotational populations resemble those predicted by the Franck–Condon model for dissociation [26]. The large recoil anisotropy parameter is also in agreement with dissociation on S_1. We note, however, that because the well depth on S_1 is small, state-specific effects in the product state distributions may be present.

4.2. Barrier to ^{1}NH + CO dissociation on S_1

The S_1 barrier height to channel (3) can be better defined by examining the near threshold ^{1}NH yield spectra and rotational distributions [10]. Near its threshold ($E_{avl} = 0$ to ≈ 500 cm^{-1}) the ^{1}NH yield is very small and increases only slowly with excess energy, as shown in fig. 4(a) of Ref. [10]. At ≈ 500 cm^{-1} above $D_0(^1$NH + CO), a sudden increase in the ^{1}NH yield is observed both in one-photon [10], and in vibrationally mediated photodissociation [9]. This increase is much larger than the gradual increase in the HNCO absorption cross section; e.g., a corresponding change in the NCO yield spectrum from channel (2) is not observed (see fig. 5 of Ref. [10]). An abrupt increase in quantum yield is anticipated when the barrier to direct dissociation on S_1 is exceeded. Moreover, the increase in the ^{1}NH yield is accompanied by a change in its rotational distribution. At the lowest excess energy examined ($E_{avl} = 135$ cm^{-1}), only $J_{NH} = 2$ is populated, as dictated by energy conservation. When E_{avl} is increased to 395 cm^{-1}, significant population also appears in $J = 3$ (see Table 1), in agreement with statistical theories for a *barrierless dissociation*. However, a pronounced change in the ^{1}NH rotational distribution occurs again at ≈ 500 cm^{-1} above $D_0(^1$NH + CO). The distribution recorded for $E_{avl} = 555$ cm^{-1} is significantly colder than that at 395 cm^{-1}, and for $E_{avl} \geq 555$ cm^{-1} the rotational excitation increases only modestly and smoothly with excess energy, as is common in *decomposition over a barrier*.

The bulk of the evidence thus suggests that below the S_1 barrier, decomposition to ^{1}NH + CO takes place on S_0 following IC to that surface; once the barrier height on S_1 is exceeded direct dissociation on S_1 via channel (3) becomes important. We place this barrier at 400–600 cm^{-1} and note that our experimental barrier height is in excellent agreement with two very recent ab initio calculations that give values of < 700 cm^{-1} [16] and 550 ± 50 cm^{-1} [17]. A barrier to dissociation on S_1 has been predicted before from a low level ab initio study that reported a 1.95 Å C–N bond length at the transition state [7].

4.3. Triplet channel dissociation

At 230.1 nm, the available energy for C–N bond cleavage via channel (1) is approx. 14000 cm^{-1}, and

calculations place the exit channel barrier height at ≈ 1800 cm^{-1} above $D_0(^3NH + CO)$ [15]. Previous experimental results show that the corresponding ^3NH rotational distribution is quite cold [13]. The triplet channel CO REMPI spectrum extracted from the imaging data (Fig. 2b) clearly peaks at low J's ($J_{CO} < 20$), but also exhibits a pronounced tail extending up to $J_{CO} \approx 60$, while the maximum allowed by energetics is $J = 82$. The appearance of the spectrum suggests at least a bimodal energy distribution, but a fit using forward convolution was not attempted. A possible explanation for the multimodal appearance of the CO rotational distribution is the participation of other triplet surfaces; for example, preliminary calculations using the Gaussian 94 package reveal a second triplet surface, $T_2(^3A')$, which is close to $T_1(^3A')$ in the Franck–Condon region of the optical excitation [27].

5. Concluding remarks

The results presented here resolve the apparent disagreement regarding the dissociation mechanism leading to channel (3) near its threshold, and the $CO(v = 0)$ rotational distribution at 230.1 nm. We conclude that at this photolysis wavelength, CO correlated with channel (3) evolves mainly on S_1, and that a large fraction of the observed $CO(v = 0)$ signal originates in channel (1). The present results are also in agreement with the available information on photofragment yield spectra, ^1NH rotational distributions and $^1NH/^3NH$ population ratios [13] [3]. Indications for increased S_1 participation at photolysis wavelengths < 230 nm are the increasing ^1NH yield, $^1NH/^3NH$ population ratios, and widths of structural features in the ^1NH yield spectra with decreasing wavelength [10–13], as well as the appearance of state-specific effects in the one-photon and the vibra-

tionally mediated photodissociation [9,13]. The rotational distributions of both CO and ^1NH are cold, indicating little angular anisotropy in the exit channel on the S_1 potential energy surface; the large translational energy release is common in dissociation over a barrier.

The suggested barrier height to S_1 dissociation is 400–600 cm^{-1} above $D_0(^1NH + CO)$, or ≈ 9000 cm^{-1} above the S_1 origin, in good agreement with theory [16,17]. Note that theoretical calculations place the barrier to channel (2) on S_1 at 8800 ± 900 cm^{-1} above $D_0(H + NCO)$, or > 12000 cm^{-1} above the S_1 origin [17], and thus at 230 nm channel (2) products are generated via radiationless decay on S_0.

Acknowledgements

References

[1] R.N. Dixon, G.H. Kirby, Trans. Faraday Soc. 64 (1968) 2002.
[2] (a) T.A. Spiglanin, R.A. Perry and D.W. Chandler, J. Phys. Chem. 90 (1986) 6184; (b) T.A. Spiglanin and D.W. Chandler, Chem. Phys. Lett. 141 (1987) 428; (c) T.A. Spiglanin, R.A. Perry and D.W. Chandler, J. Chem. Phys. 87 (1987) 1568; (d) T.A. Spiglanin and D.W. Chandler, J. Chem. Phys. 87 (1987) 1577.
[3] W.K. Yi, R. Bersohn, Chem. Phys. Lett. 206 (1993) 365.
[4] B. Bohn, F. Stuhl, J. Phys. Chem. 97 (1993) 4891.
[5] B. Ruscic, J. Berkowitz, J. Chem. Phys. 100 (1994) 4498.
[6] J. Zhang, M. Dulligan, C. Wittig, J. Phys. Chem. 99 (1995) 7446.
[7] W.-H. Fang, X.-Z. You, Z. Yin, Chem. Phys. Lett. 238 (1995) 236.
[8] M. Kawasaki, Y. Sato, K. Suto, Y. Matsumi, S.H.S. Wilson, Chem. Phys. Lett. 251 (1996) 67.
[9] S.S. Brown, R.B. Metz, H.L. Berghout, F.F. Crim, J. Phys. Chem. 105 (1996) 6293.

---

[3] The relative CO populations from channels (3) and (1) cannot be extracted from the imaging data which are recorded only for $CO(v = 0)$, whereas $v = 1$ and 2 are also produced [20]. Also, the $CO(B^1\Sigma^+)$ state is predissociative for $J > 37$. A reliable value for the branching ratio was obtained from LIF measurements of the ^1NH and ^3NH fragments, which give a $^1NH/^3NH$ population ratio of ≈ 0.2 at 230.0 nm [13].

[10] M. Zyrianov, A. Sanov, Th. Droz-Georget, H. Reisler, J. Chem. Phys. 105 (1996) 8111.

[11] Th. Droz-Georget, M. Zyrianov, A. Sanov, H. Reisler, Ber. Bunsenges. Phys. Chem. 101 (1997) 469.

[12] A. Sanov, Th. Droz-Georget, M. Zyrianov, H. Reisler, J. Chem. Phys. 106 (1997) 7013.

[13] M. Zyrianov, Th. Droz-Georget, H. Reisler, J. Chem. Phys. 106 (1997) 7454.

[14] (a) R.A. Brownsword, T. Laurent, R.K. Vatsa, H.-R. Volpp and J. Wolfrum, Chem. Phys. Lett. 249 (1996) 162; (b) ibid. 258 (1996) 164; (c) R.A. Brownsword, M. Hillenkamp, T. Laurent, R.K. Vatsa and H.-R. Volpp, J. Chem. Phys. 106 (1997) 4436.

[15] A.M. Mebel, A. Luna, M.C. Lin, K. Morokuma, J. Chem. Phys. 105 (1996) 6439.

[16] J.E. Stevens, Q. Cui and K. Morokuma (to be published).

[17] J. Klossika, H. Floethmann, C. Beck, R. Schinke and K. Yamashita, Chem. Phys. Lett. (submitted).

[18] (a) D.W. Chandler and P.L. Houston, J. Chem. Phys 87 (1987) 1445; (b) A.J.R. Heck and D.W. Chandler, Annu. Rev. Phys. Chem. 46 (1995) 335.

[19] (a) D.H. Parker and A. Eppink, J. Chem. Phys. (in press); (b) ibid. Rev. Sci. Instrum. (submitted).

[20] Th. Droz-Georget, M. Zyrianov and H. Reisler (unpublished).

[21] P.J.H. Tjossem, K.C. Smyth, J. Chem. Phys. 91 (1989) 2041.

[22] A. Ogai, C.X. Qian, H. Reisler, J. Chem. Phys. 93 (1990) 1107.

[23] R.N. Bracewell, in: The Fourier Transform and its Applications (McGraw-Hill, New York, 1986).

[24] A.L.L. East, C.S. Johnson, W.D. Allen, J. Chem. Phys. 98 (1993) 1299.

[25] (a) P. Pechukas and J.C. Light, J. Chem. Phys. 42 (1966) 794; (b) P. Pechukas, J.C. Light and C. Rankin, ibid. 44 (1966) 794; (c) J.C. Light, Discuss. Faraday Soc. 44 (1996) 14.

[26] R. Schinke, in: Photodissociation Dynamics (Cambridge University Press, 1993).

[27] M. Zyrianov, A. Sazonov, R.A. Beaudet and H. Reisler (to be published).